Supplementary Information

Screening-enhanced effect enables poly(hexamethylene biguanide) hydrochloride to effectively overcome charge screening limitations

Chun Yang[1], Peng Liu[1], Peng Tao[1], Haijie Cao[2], Ka-Fu Yung[1,*], Chi-Wai Kan[3,*], & Wen-Yi Wang[1,*]

[1]Department of Applied Biology and Chemical Technology, The Hong Kong Polytechnic University, Hong Kong, China.

[2]Institute of Materials for Energy and Environment, School of Materials Science and Engineering, Qingdao University, Qingdao 266071, China.

[3]School of Fashion and Textiles, The Hong Kong Polytechnic University, Hong Kong, China.

*Correspondence: kf.yung@polyu.edu.hk (KFY); kan.chi.wai@polyu.edu.hk (CWK); wang.wenyi@polyu.edu.hk (WYW)

This file concludes:

Supplementary Figs. 1 to 22

Supplementary Tables 1 to 4

Supplementary Notes 1 to 14

Supplementary Equations 1 to 16

Supplementary References 1 to 64

Supplementary Note 1 Flocculation experiments of PHMB

To measure the flocculation ability of PHMB in treating dyeing wastewater, a typical dye (C.I. Reactive Red 24) was selected to simulate real dyeing wastewater. Commercial Levafix Blue CA and Levafix Yellow CA reactive dyes were also employed to ensure the reliability of the results. The stock solution of PHMB of a concentration of 1000 mg·L^{-1} was prepared from high-purity polymer powder. Different volumes of PHMB solution and ultrapure water were transferred into a series of centrifuge tubes. The total volume was 20 mL after injecting 10 mL of dye solution at a concentration of 200 mg·L^{-1}. The PHMB concentration gradient was designed as 5, 10, 15, 20, 30, 40, 50, 60, 70, and 80 mg·L^{-1} for the final reaction solution. After allowing the sample to stand for approximately 5 hours, 15~20 mL of the supernatant was extracted and reserved for subsequent examination in a neutral solution environment at room temperature.

Firstly, 10 mL of the supernatant was used for turbidity measurement using the Orion™ AQUAfast AQ3010 Turbidity Meter (Thermo Fisher Scientific Inc.). After that, about 2 mL remaining supernatant was drawn with a syringe and filtered through a 0.45 μm pore size filter. The resulting filtrate was subjected to absorbance measurements (UV-2401PC UV/visible spectrophotometer (Shimadzu Corporation)) at the wavelengths of 510 nm, 611 nm, and 420 nm to test the absorbance of the red, blue, and yellow dyes, respectively. The color removal efficiency R (%) was determined using the following equation:

$$R\ (\%) = \frac{C_0 - C_1}{C_0} \times 100\% \qquad (1)$$

Where C_0 represented the initial concentration of the dye, and C_1 represented the concentration after flocculation. The turbidity and decoloration efficiency results were shown simultaneously in Supplementary Figs. 1a, 1c to verify the flocculation ability of PHMB. With the concentration gradually increasing to 50 mg·L^{-1}, the decolorization rate of dye wastewater gradually reached 100%, which indicated that all the dyes had completely flocculated at this concentration.

In addition, the zeta potential of the fully settled supernatant was also measured and analyzed by a zeta sizer advance system (Malvern Panalytical Company), as shown in Supplementary Figs. 1a, 1c (inset). Notably, the turbidity of the dyes saw a peak value at which the zeta potential hit a minimum value. After surpassing the peak point, the turbidity tended to be flat, while the zeta potential showed a nearly linear increment with increasing PHMB concentration. This phenomenon signified that excessive PHMB could disintegrate the flocculated particles due to the charge accumulation on the particles, leading to particle repulsion and redispersion.

To investigate the impact of a highly saline environment on the flocculation performance of PHMB, different weights of NaCl crystals were added in advance to make the concentrations of the salt 1, 5, 25, 50, 100, 150, 200, 250, 300, 400, and 500 mmol·L^{-1}, respectively. As shown in Supplementary Figs. 1b, 1d, while maintaining a constant concentration of 20 mg·L^{-1} of PHMB, the color removal efficiency increased with increasing salt concentration until 100% efficiency was reached. Levafix Yellow CA and Levafix Blue CA needed 150 and 250 mmol L^{-1} NaCl for a complete flocculation, respectively.

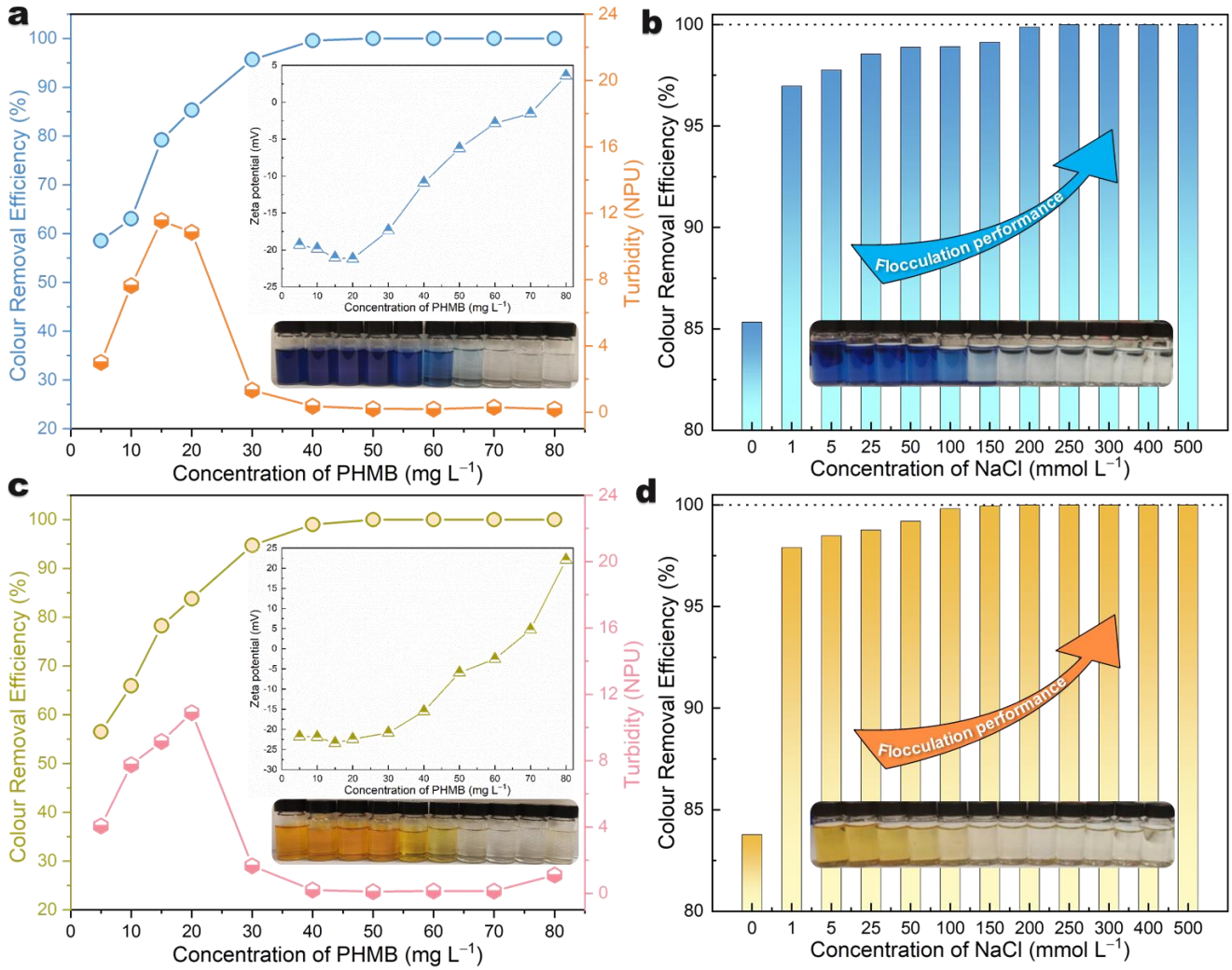

Supplementary Fig. 1 Flocculation ability of PHMB in treating dyeing wastewater. Decoloration efficiency and turbidity curves with varying PHMB concentrations for Levafix Blue CA **(a)** and Levafix Yellow CA **(c)**. Curves of zeta-potential with varying PHMB concentrations for Levafix Blue CA and Levafix Yellow CA active dyes also have been exhibited (inset). While maintaining a constant concentration of 20 mg•L^{-1} of PHMB, the color removal efficiency increased as salt concentrations increased for Levafix Blue CA **(b)** and Levafix Yellow CA **(d)**, respectively.

Supplementary Note 2 DFT Computational methods

The preliminary optimized structures were obtained using the Gaussian16 software with B3LYP-GD3BJ functional and DFT-D3 method with Becke-Jonson damping[1–6], and the TZVP basis set was used in this step for sufficient accuracy[7,8]. The NBO program was used to generate the required output files[9–17]. To more precisely analyse noncovalent interactions of main group elements, M06-2X density functional and ma-diffuse def2-TZVP basis sets with dispersion remedy were adopted for single-point energy calculation[18–22]. These simulations also introduced the SMD (Solvation Model Based on Density) implicit solvent model to treat the liquor part involved[23]. Meanwhile, the ab initio program VASP (Vienna Ab initio Simulation Package) was used to rapidly obtain rough results at the outset [24,25], and the generalized gradient approximation (GGA) of the Perdew-Burke-Ernzerh(PBE) method was employed [26,27]. Energy cutoffs of 450 eV and a convergence threshold of 0.01 eV $Å^{-1}$ for forces were set. The DFT-D3 method (Becke-Jonson damping) was utilized for correcting the van der Waals interactions [5,6], and it was coupled with the VASPsol solvation module (setting the dielectric constant as 80 F m^{-1}) for correcting the solvent effect[28,29]. Considering the charged nature of the molecules, the count of the total valence electrons must be specified in the program. A uniform (1×1×1) *k*–mesh sampling scheme was employed for all structures and *k*–points were generated by the Monkhorst-Pack method. Subsequent analyses primarily relied on the results obtained from Gaussian software supplemented by wave function analysis using the Multiwfn program[30]. Unless otherwise specified, data obtained from the Gaussian software were processed by the Multiwfn program and visualized using the VMD (Visual Molecular Dynamics) software[31]; Results obtained from the VASP package were typically visualized using the VESTA (Visualisation for Electronic Structural Analysis) program[32].

Supplementary Note 3

To verify the stable configuration of protonated PHMB in the aqueous solution, we conducted simulations to obtain the energy barriers of the PHMB protonation reactions and the stability of various possible configurations. The energy of protonation was defined as:

$$E_p = E_{PHMB-H^+} - (E_{PHMB} + E_{H^+}) \quad (2)$$

$$E_{p'} = E_{PHMB-2H^+} - (E_{PHMB-H^+} + E_{H^+}) \quad (3)$$

$$E_{2p} = E_{PHMB-2H^+} - (E_{PHMB} + 2E_{H^+}) \quad (4)$$

in which E_p, $E_{p'}$, and E_{2p} were the energy barriers of the protonation reactions while the first proton, the second proton, and two protons were inserted, respectively. Additionally, E_{H^+}, E_{PHMB-H^+}, and $E_{PHMB-2H^+}$ represented the ground state energy of a proton ion, the mono-protonated PHMB monomer,

and the bi-protonated PHMB monomer, respectively. As shown in Supplementary Fig. 2, the energy calculation showed that only a monoproto-PHMB (mono-protonated PHMB monomer) could exist in a stable state. Therefore, a PHMB monomer that adsorbed more than one proton was unstable.

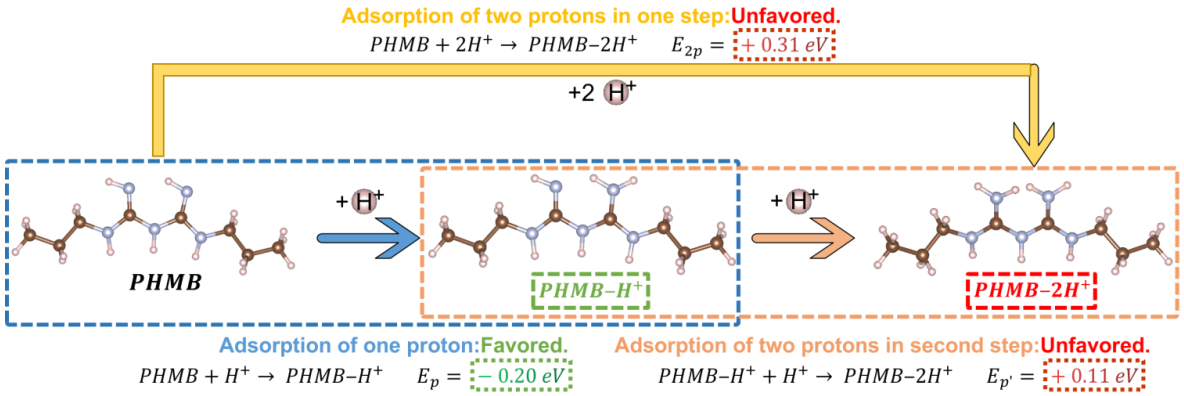

Supplementary Fig. 2 Protonation of PHMB monomer and stability of different protonation states. The color brown represents C, pink for H, and cyan for N atoms.

Supplementary Note 4

Thus, given the diverse configurations of PHMB, as shown in Supplementary Fig. 3c, the initial focus of this study was to confirm the most stable molecular type. The energy differences of PHMB monomers in water (implicit solvent model) were calculated by using the Gaussian16 quantum chemistry program and ab initio quantum chemistry package VASP, as shown in Supplementary Figs. 3a, 3b, respectively. The calculation methods and accuracy requirements for structural optimization and single-point energy calculation were as mentioned above. After conversion (1 eV = 23.06 kcal·mol^{-1}), similar results were obtained from the two simulation methods, and the same trend was observed by the two methods, i.e., the stability of mono-protonated PHMB: Type II > Type I > Type III (Supplementary Fig. 3d).

The flocculation complexes were constructed based on the stable PHMB monomer model. The adsorption energy of a cationic PHMB monomer targeting a dye molecule was defined as:

$$E_f = E_{xy\cdot PHMB^+ - x\cdot dye^{y-}} - (xy\cdot E_{PHMBH^+} + x\cdot E_{dye^{y-}}) \qquad (5)$$

In this formula, E_f was defined as the energy barrier of flocculation. E_{PHMBH^+}, $E_{dye^{y-}}$, and $E_{xy\cdot PHMB^+ - x\cdot dye^{y-}}$ referred to the ground state energy of the PHMB monomer, the Levafix Red CA dye molecule, and their flocculated complex, respectively, in which x and y were charge values.

As illustrated in Supplementary Fig. 3e, considering the different binding configurations, the values of E_f of the two distinct binding models were calculated under equivalent simulation conditions and convergence criteria. The computed energy barrier for the parallel adsorption complex was -0.57 eV. In contrast, the vertical-adsorption model exhibited a significantly lower energy barrier with a value of -

0.32 eV. A more stable parallel-adsorption structure implied a compact binding trend between PHMB and the dye molecule. In addition, when using Gaussian software, we consistently obtained a structure similar to the parallel adsorption model, and the values of single-point energy were also close to each other.

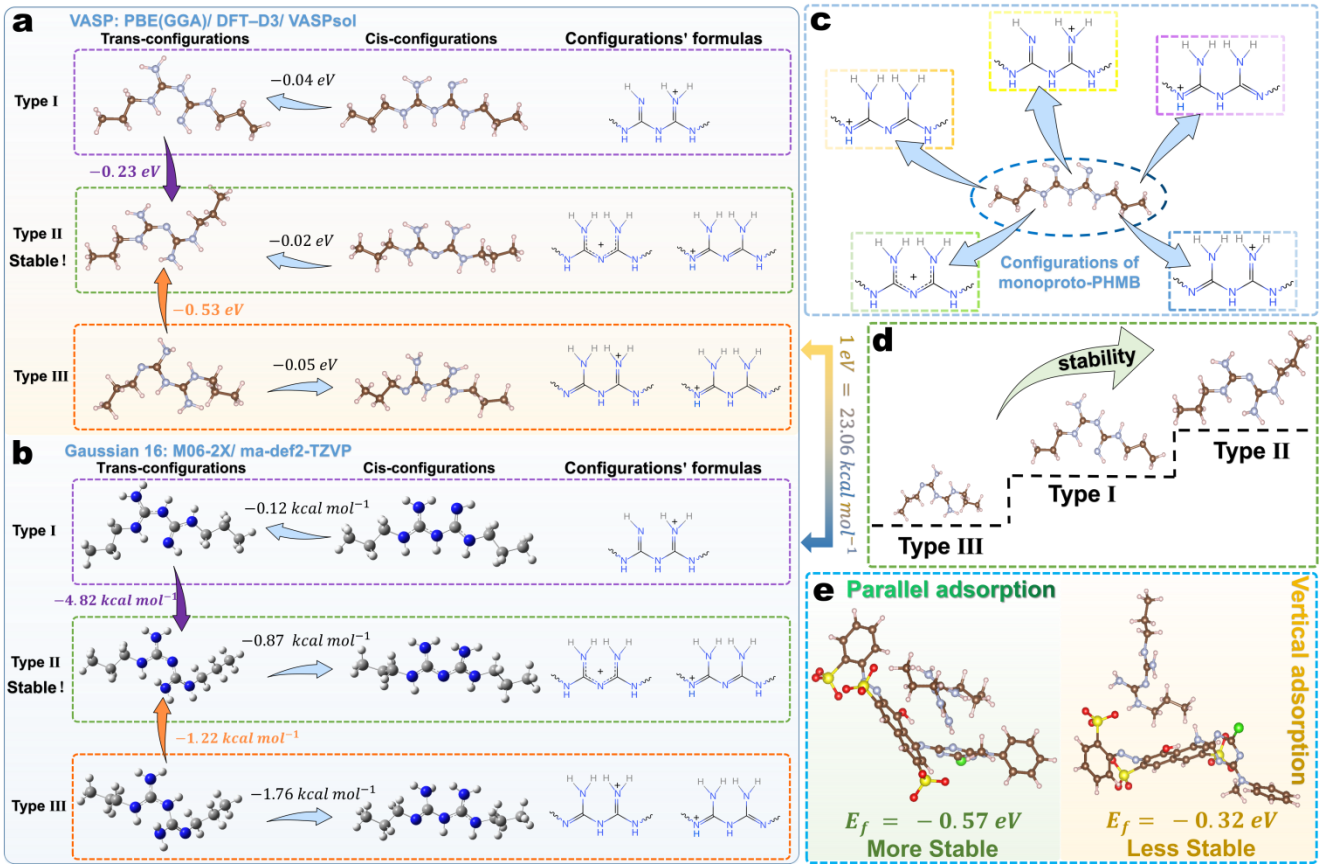

Supplementary Fig. 3. (a) Energy differences between different configurations of the PHMB monomer, calculated by quantum chemistry software VASP based on GGA with PBE method, DFT-D3 London-dispersion correction, and VASPsol package; **(b)** Configurations' energy differences calculated from DFT method with dispersion basis by software Gaussian 16 based on M06-2X density functional, ma-diffuse def2-TZVP basis sets and SMD implicit solvent model; **(c)** Possible configurations of the mono-protonated PHMB monomer; **(d)** Stability ranking of different configurations; **(e)** Energy barriers of flocculation of parallel and vertical adsorption configurations, respectively. The color brown stands for C, yellow for S, red for O, pink for H, and cyan for N **(a, d, e)**. Grey stands for C, blue for N, and white for H **(b)**.

Supplementary Note 5

Based on the simulation results derived from the calculation by Gaussian 16 software, electrostatic potential maps (Supplementary Fig. 4) and charge distributions (Supplementary Figs. 5, 6) were further

obtained. The Bader charge[33–36] and DDEC6[37–43] charge distribution of the PHMB monomer were also presented in Table 1, by the self-consistent field outcomes obtained from VASP calculations, with the corresponding atom indices shown in Supplementary Fig. 7. To better analyze and visualize the distribution of electrostatic potential, the van der Waals surface (defined by Bader, wherein the isosurface of electron density at 0.001 a.u. was considered as the van der Waals surface[44,45]) images and the van der Waals surface penetration graph were shown in Fig. 2b and Supplementary Fig. 8.

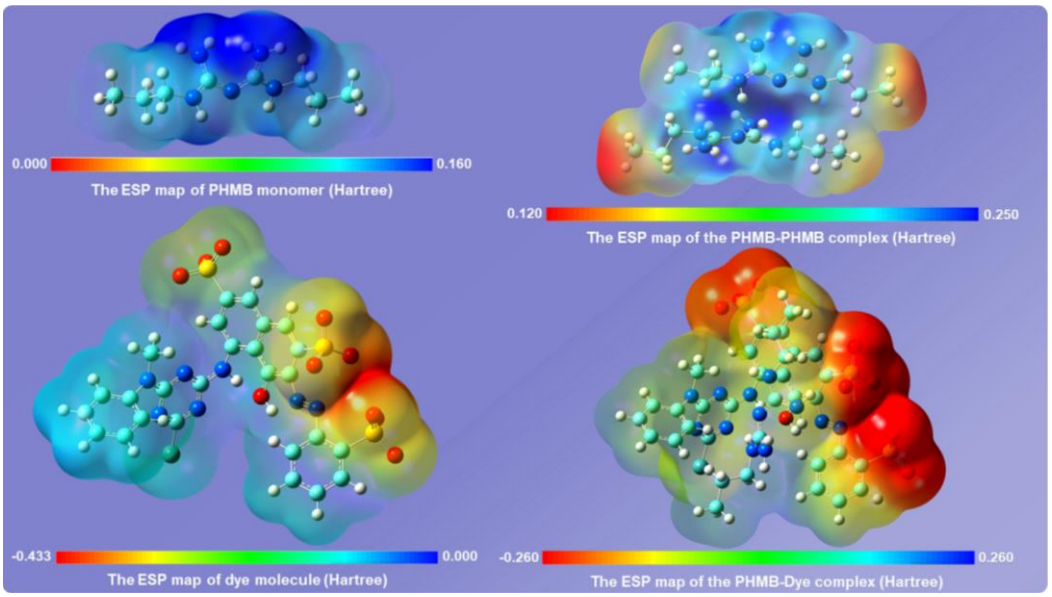

Supplementary Fig. 4 ESP maps of the dye molecule, PHMB monomer, and their complex calculated by Gaussian 16 and drawn by GaussView[46]. The regions closer to red exhibited more negative electrostatic potential values, whereas those closer to blue corresponded to more positive ones[47–49]. Blue stands for N, yellow for S, red for O, white for H, and cyan for C.

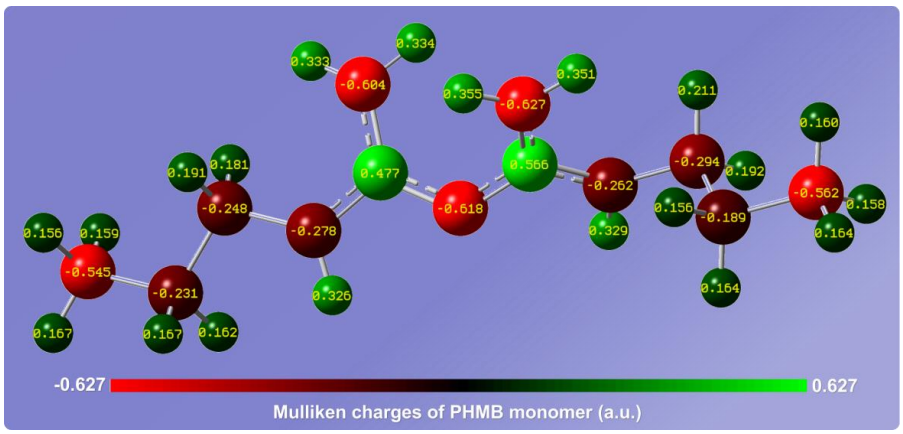

Supplementary Fig. 5 Mulliken charges of the PHMB monomer calculated by Gaussian 16 and drawn by GaussView. Shifting toward red indicated increased atomic charge negativity, while shifting toward green signified increased atomic charge positivity[50]. The arrangement of each atom corresponded to the respective molecule shown in Supplementary Fig. 4.

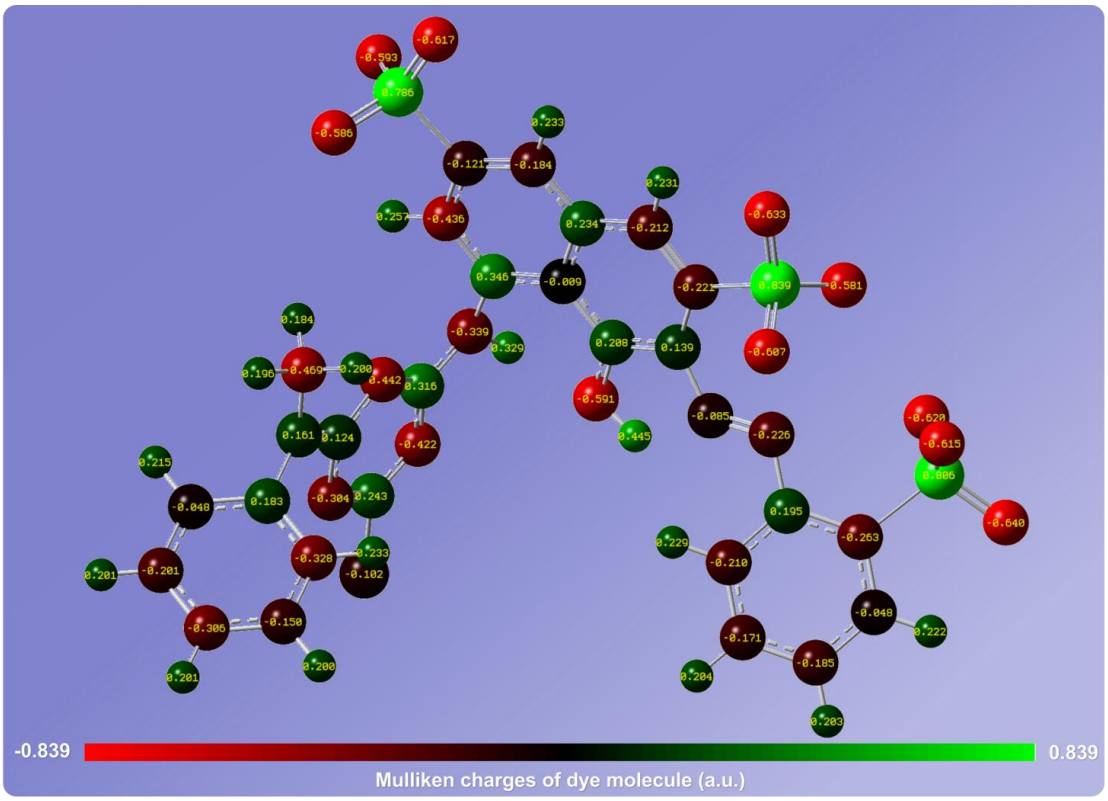

Supplementary Fig. 6 Mulliken charges of the dye molecule calculated by Gaussian 16 and drawn by GaussView. Shifting toward red indicated increased atomic charge negativity, while shifting toward green signified increased atomic charge positivity. The arrangement of each atom corresponded to the respective molecule shown in Supplementary Fig. 4.

Supplementary Table 1 The Bader charge and DDEC6 charge distribution of PHMB monomer, using the VTST Tools[51], Bader add-ons[33], VASPKIT code[52], and Chargemol program[53], based on the self-consistent field results by VASP.

Atoms	Bader charge	DDEC6 charge
N1	-1.277233	-0.669036
N2	-1.250728	-0.399147
N3	-1.294274	-0.384751
N4	-1.325277	-0.640277
N5	-1.340351	-0.704969
C1	0.305309	-0.001928
C2	-0.025874	-0.119285
C3	-0.137022	-0.361820
C4	1.682151	0.616058
C5	1.626789	0.613575
C6	0.289569	0.003471
C7	-0.025418	-0.126958
C8	-0.099591	-0.364737

H1	0.49919	0.369544
H2	0.050594	0.084060
H3	0.070243	0.086654
H4	0.029333	0.089539
H5	0.035700	0.091800
H6	0.069656	0.113389
H7	0.037326	0.114858
H8	0.060475	0.120382
H9	0.537372	0.316629
H10	0.52743	0.383209
H11	0.542595	0.383573
H12	0.554688	0.334739
H13	0.098826	0.080268
H14	0.062445	0.083873
H15	0.043902	0.084063
H16	0.013628	0.080019
H17	0.035057	0.114771
H18	0.038316	0.112363
H19	0.030316	0.118377
H20	0.534856	0.377695
Total	0.999998	1.000001

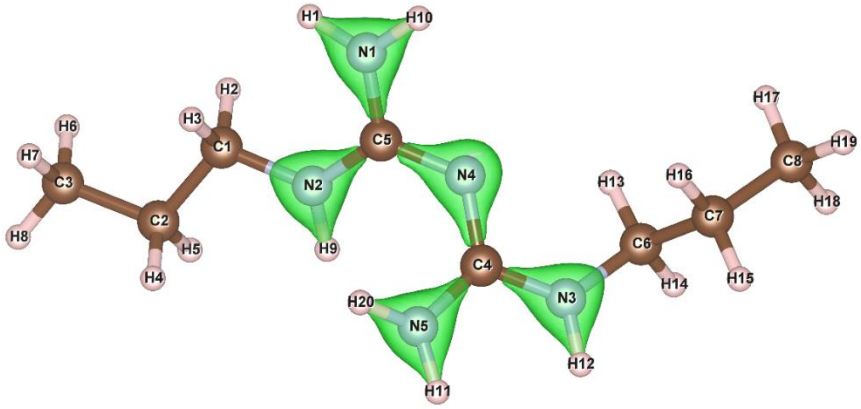

Supplementary Fig. 7 Geometrical structures and electron-density isosurface of PHMB monomer (isosurface level = 0.3 e•bohr^{-3}). The number tag of each atom corresponded to the atom tag in Table 1. The color brown stands for C, pink for H, and cyan for N atoms. The green translucent electron density isosurface at 0.3 e•bohr^{-3} indicated that the N atom was an electron-rich region.

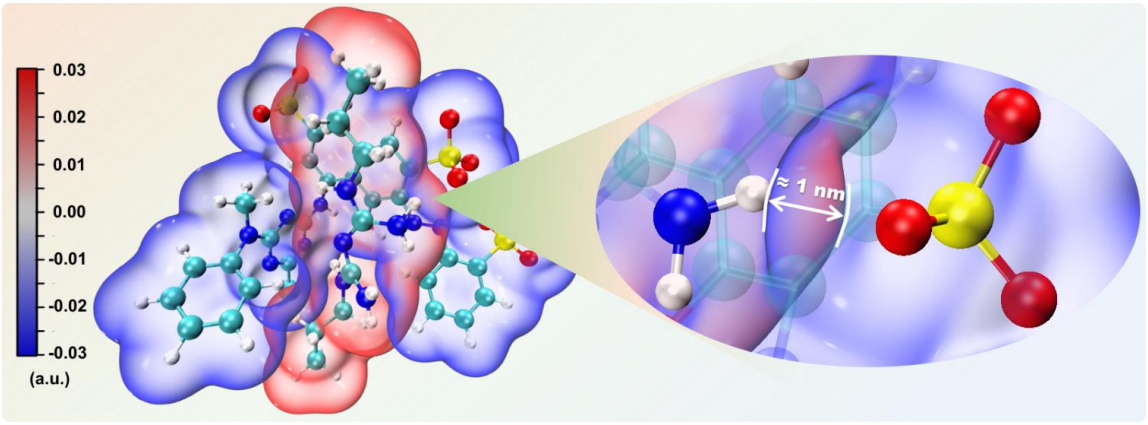

Supplementary Fig. 8 Schematic van der Waals penetration distance between the biguanide group and the sulfonic acid group. The mutual penetration is 2 nm according to its definition (two times the corresponding penetration distance).

Supplementary Note 6

In the next step, the RDG (Reduced Density Gradient) function in wave function analysis was applied to allow for a meticulous delineation of regions manifesting weak interactions. The RDG function was defined in Supplementary Equation (6)[54]:

$$s(RDG) = \frac{|\nabla\rho(r)|}{2\times\sqrt[3]{3\times\pi^2\times\sqrt[3]{\rho(r)^4}}} \qquad (6)$$

Where $\rho(r)$ was the electron density, and $|\nabla\rho(r)|$ was the modulus of the electron density gradient[54,55]. The existence of spike lines of the RDG $vs.$ $\rho(r)$ pattern indicated that the system has weak interactions. The isosurface could be visualized to determine the positions of corresponding regions, and reveal the weak interaction in real space, as shown in Supplementary Figs. 9, 10.

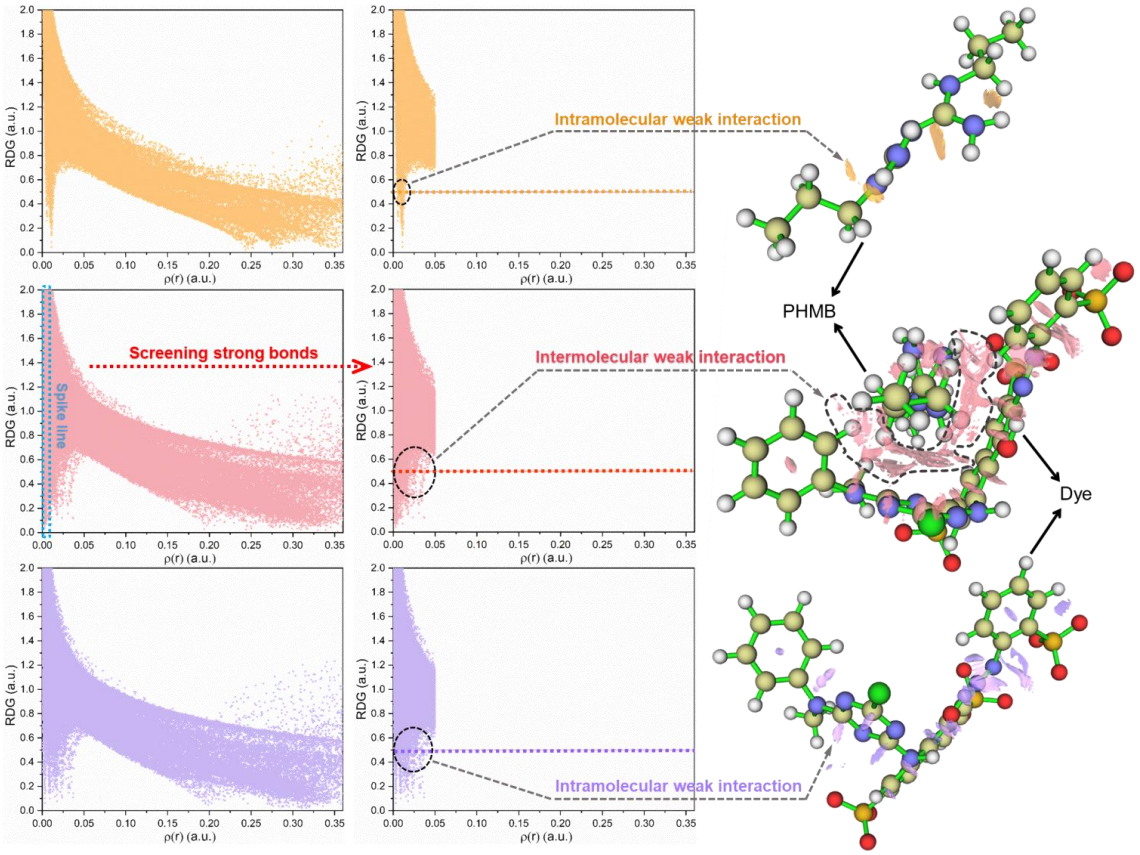

Supplementary Fig. 9 The complete RDG-$\rho(r)$ scatter diagram in the $\rho(r)$ range of (0.00, 0.35) (left); The RDG-$\rho(r)$ scatter diagram in the case of shielding strong chemical bonds (center); The corresponding intermolecular or intramolecular colored regions (right). In these representations, carbon (C) atoms are depicted in yellow, nitrogen (N) atoms in blue, sulfur (S) atoms in deep yellow, oxygen (O) atoms in red, hydrogen (H) atoms in white, and chlorine (Cl) atoms in green.

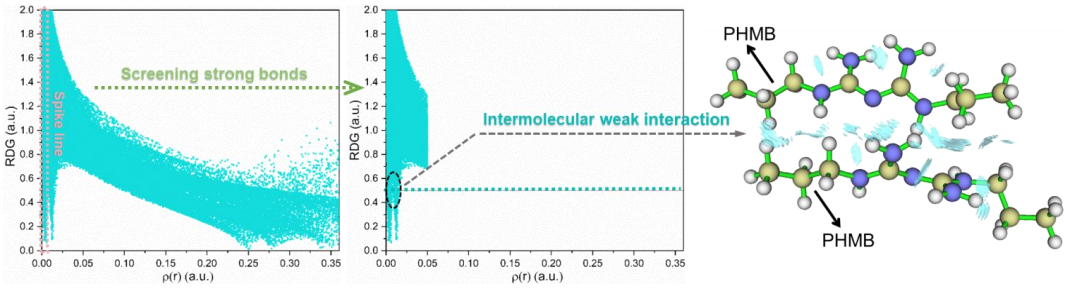

Supplementary Fig. 10 The complete RDG-$\rho(r)$ scatter diagram in the $\rho(r)$ range of (0.00, 0.35) (left); The RDG-$\rho(r)$ scatter diagram in the case of shielding strong chemical bonds (center); The corresponding intermolecular colored regions (right). In these representations, carbon (C) atoms are depicted in yellow, nitrogen (N) atoms in blue.

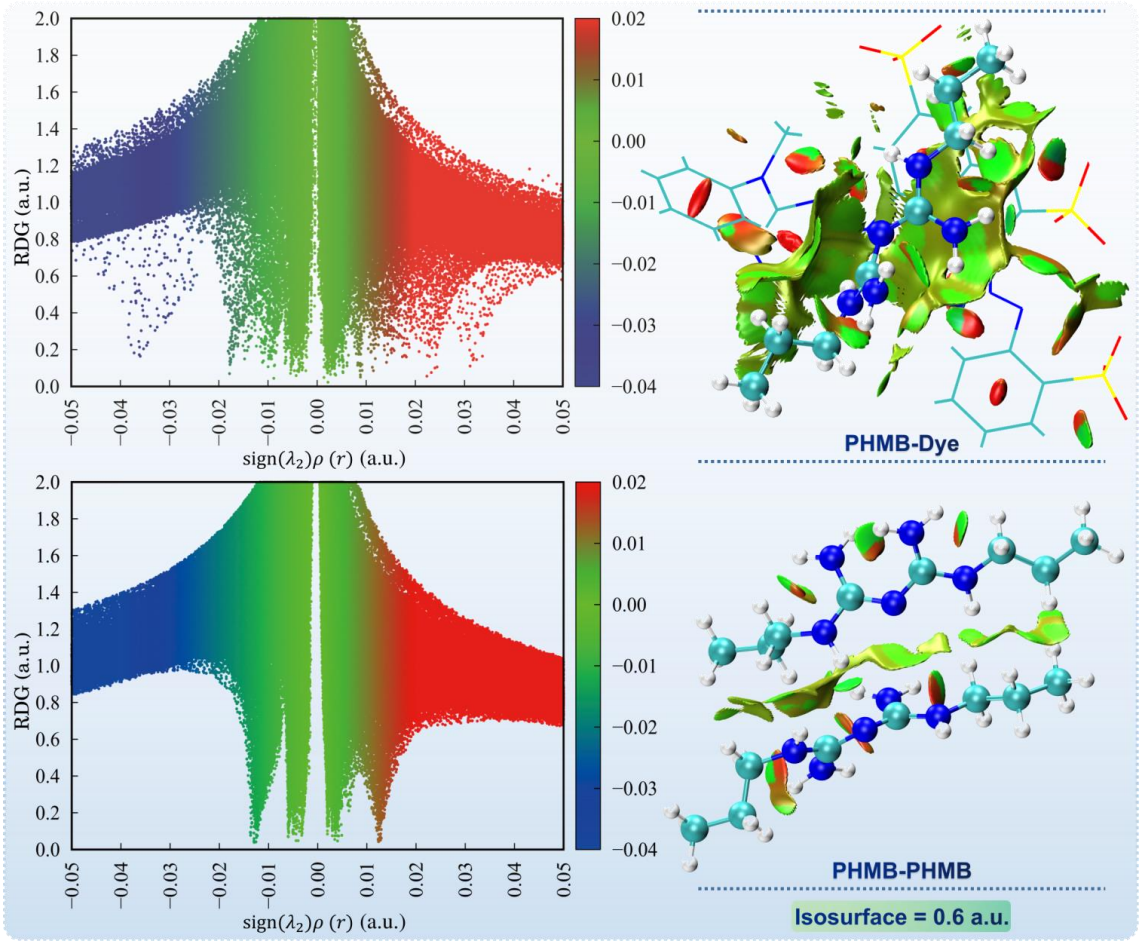

Supplementary Fig. 11 The RDG-$sign(\lambda_2)\rho(r)$ scatter diagrams and the corresponding colored regions.

Supplementary Note 7

By the IGMH (Independent Gradient Model based on Hirshfeld partition) method, the electron density of each atom was divided by the Hirshfeld atomic space according to the actual electronic structure and chemical environment[56–58]. δg was defined in Supplementary Equation (7)[56,57]:

$$\delta g(r) = \sum_i \left|\nabla \rho_i^{Hirsh}(r)\right| - \left|\sum_i \nabla \rho_i^{Hirsh}(r)\right| = g^{IGMH} - g(r) \qquad (7)$$

where $\rho_i^{Hirsh}(r)$ represented the actual electron density of atoms calculated by the quantum chemistry method or determined by crystal diffraction experiments. i and r were the Cartesian coordinate vectors. Thus, the $\delta g^{inter}(r)$ specifically denoted the interactions between fragments, as defined in Supplementary Equation (8)[57,58]:

$$\delta g^{inter}(r) = \sum_A \left|\sum_{i \in A} \nabla \rho_i^{Hirsh}(r)\right| - \left|\sum_A \sum_{i \in A} \nabla \rho_i^{Hirsh}(r)\right| = g^{IGMH,inter}(r) - g^{inter}(r) \qquad (8)$$

Where 'A' represented the molecular fragments looping the system, and 'i' represented the atoms looping the corresponding fragment[57]. The isosurfaces of $\delta g^{inter}(r)$ or corresponding scatter plots colored by

$sign(\lambda_2)\rho^{Hirsh}(r)$ function could more accurately exhibit the weak-interaction areas between two fragments, as shown in Fig. 2 and Supplementary Figs. 12, 13. Furthermore, the IGMH method could facilitate quantitative analysis of interactions between fragments, such as the atomic pair δg index (δg^{pair}), which was defined as follows[57]:

$$\delta g_{i,j}^{pair} = \int g_{i,j}(r)dr = \int \left[g_{i,j}^{IGMH}(r) - g_{i,j}(r)\right] dr \quad i \in A, j \in B \qquad (9)$$

$$\delta g_{i,j}(r) = \left|\nabla\rho_i^{Hirsh}(r) + \nabla\rho_{i,j}^{Hirsh}(r)\right| \qquad (10)$$

$$g_{i,j}^{IGMH}(r) = \left|\nabla\rho_i^{Hirsh}(r)\right| + \left|\nabla\rho_j^{Hirsh}(r)\right| \qquad (11)$$

where A and B represented the two fragments requiring investigation, and i and j corresponded to atoms within these respective fragments. Subsequently, the contribution values of the respective atomic pairs to the total intermolecular interactions could be quantified using percentage metrics as[57]:

$$\delta g_{i,j}^{pair}(\%) = \frac{\delta g_{i,j}^{pair}}{\sum_{k\in A}\sum_{l\in B}\delta g_{k,l}^{pair}} \times 100\% \qquad (12)$$

where k or l corresponded to an atom within respective A or B fragment. Additionally, δg^{atom} could be utilized to quantitatively assess the significance of each atom in the overall inter-fragment interactions, as illustrated by Supplementary Equation (13)[57]:

$$\delta g_i^{atom} = \sum_{j\in B}\delta g_{i,j}^{pair} \qquad (13)$$

in which the contribution of atom i in fragment A to the total inter-fragment interactions could be denoted as δg_i^{atom}, and its percentage contribution could be calculated as Supplementary Equation (14)[54]:

$$\delta g_i^{atom}(\%) = \frac{\delta g_i^{atom}}{\sum_{j\in A}\delta g_j^{atom}} \times 100\% \qquad (14)$$

by which each atom could be colored based on its $\delta g_i^{atom}(\%)$, as shown in Figs. 2c, 2f and Supplementary Figs. 14, 15.

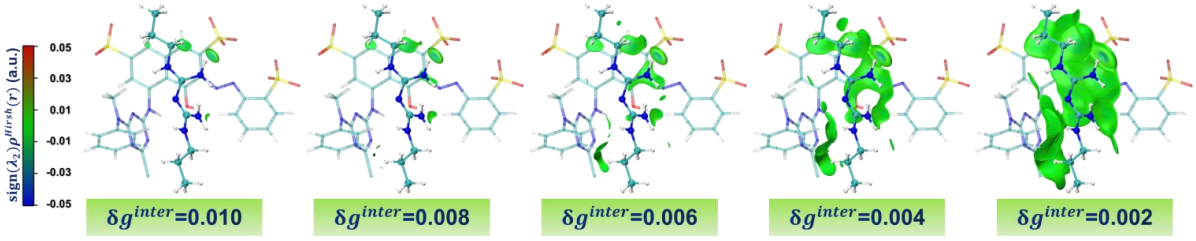

Supplementary Fig. 12 IGMH graphs with varying δg^{inter} values (within the range of $sign(\lambda_2)\rho^{Hirsh}(r)$ from -0.05 to 0.05), reflecting the regions of weak interactions. Notably, as the δg^{inter} threshold was diminished to 0.002 a.u. (farthest right one in the figure), more areas reflecting weak van der Waals interactions were projected onto the isosurface. Whereas increasing δg^{inter} to

0.01 a.u. (farthest left one in the figure), the areas reflecting weak interactions were reduced to the vicinity of the biguanide segment.

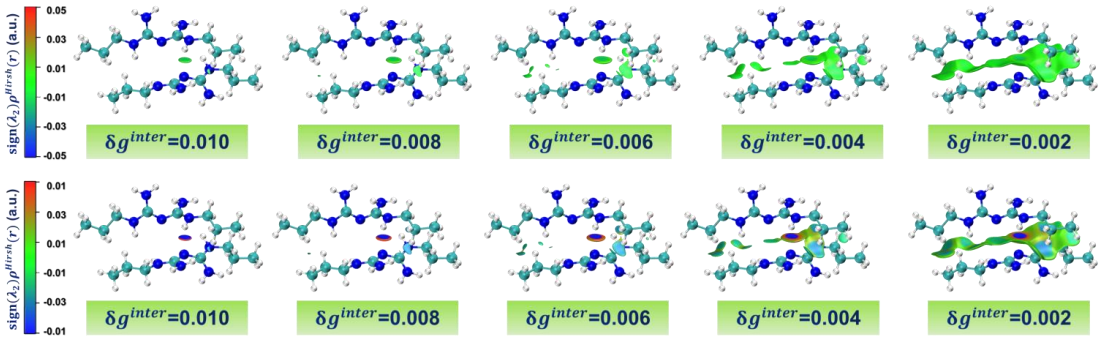

Supplementary Fig. 13 IGMH graphs with varying δg^{inter} values (within the range of $sign(\lambda_2)\rho^{Hirsh}(r)$ from -0.05 to 0.05), reflecting the regions of weak interactions. Notably, as the δg^{inter} threshold was diminished to 0.002 a.u. (farthest right one in the figure), more areas reflecting weak van der Waals interactions were projected onto the isosurface. Whereas increasing δg^{inter} to 0.01 a.u. (farthest left one in the figure.), the areas reflecting weak interactions were reduced to the vicinity of the biguanide segment.

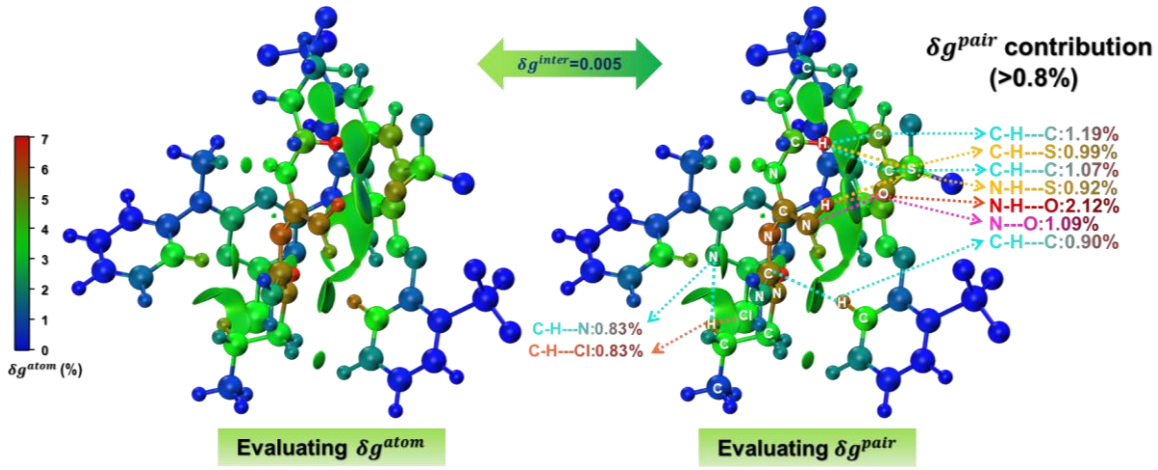

Supplementary Fig. 14 Each atom was color-coded based on its atomic δg index contribution δg^{atom} (%) as defined in Supplementary Equation (13), at δg^{inter} isosurface of 0.005 a.u. (left). A closer proximity to red indicated a higher contribution of the atom to the total interactions, while a closer proximity to blue suggested a more minor contribution. Main atom pairs (δg^{pair} contribution percentage > 0.8 %) that could be considered as A(N, C)–H···B(S, N, O, C, Cl) hydrogen bonds (right).

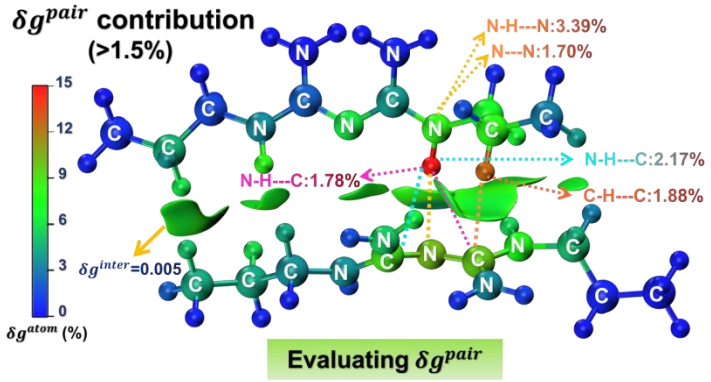

Supplementary Fig. 15 Each atom was color-coded based on its atomic δg index contribution δg^{atom} (%). A closer proximity to red indicated a higher contribution of the atom to the total interactions, while a closer proximity to blue suggested a more minor contribution. Main atom pairs (δg^{pair} contribution percentage > 1.5 %) have been marked.

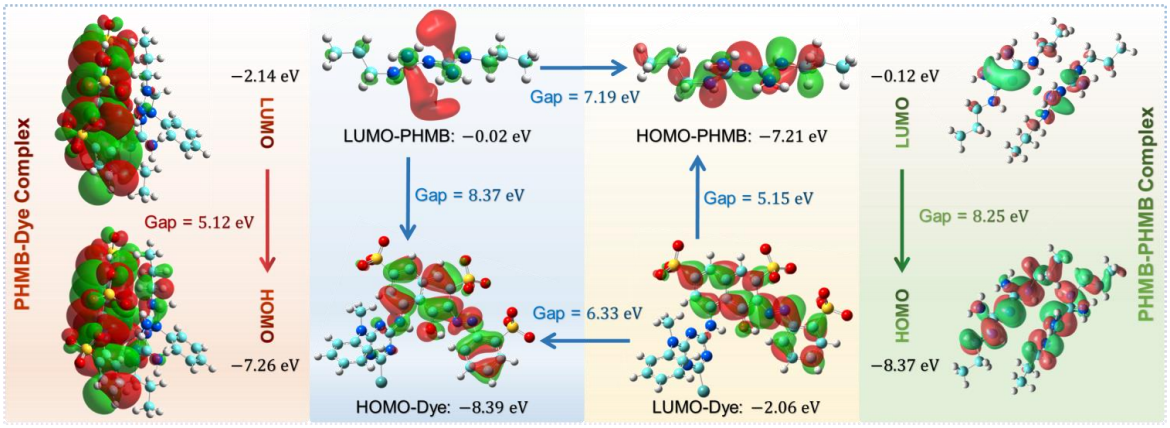

Supplementary Fig. 16 HOMO-LUMO orbital diagrams and corresponding energy levels of the dye molecule, the PHMB monomer, and their complex (calculated by Gaussian software and drawn by GaussView).

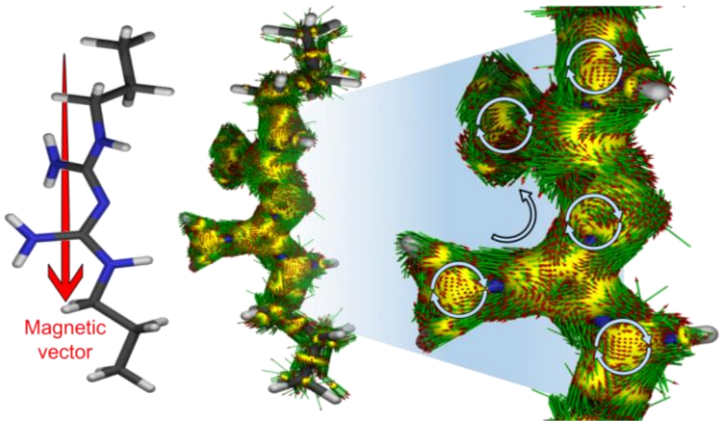

Supplementary Fig. 17 The AICD (Anisotropy of the Induced Current Density) diagram of the PHMB monomer. The AICD program[59] was employed and a magnetic field was applied to the molecule. The resulting AICD grid data were subsequently visualized as the AICD map by the POV-Ray renderer. Yellow areas were the AICD isosurfaces; Red Arrows were the induced current density vectors; Green Arrows were the magnetic field directions. Blue cycles indicated partial aromaticity around N atoms, and the semi-circle indicated overall aromaticity of the biguanide segment. The aromaticity came with delocalized electrons. Black stands for C, blue for N, and white for H.

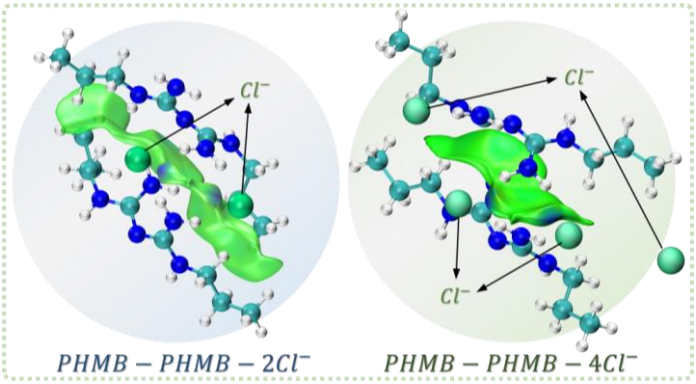

Supplementary Fig. 18 The isosurfaces of δg^{inter} at 0.001 a.u. between two fragments (each PHMB monomer as a fragment) were displayed at different Cl^- ion ratios.

Supplementary Table 2 The sobEDAw results for configurations of PHMB-Dye adsorption and PHMB-PHMB stacking complexes.

Configurations	sobEDAw B3LYP-D3(BJ)/6-311+G(2d,p) w.CB (kcal/mol)							
	ΔG_{bond}	ΔE_{int}	ΔE_{els}	ΔE_{xrep}	ΔE_{orb}	ΔE_{disp}	ΔE_{int}^{sol}	ΔCDS
PHMB-Dye	-25.13	-173.78	-150.67	40.26	-20.08	-43.29	148.65	-2.31
PHMB(Cl^-)-Dye($3Na^+$)	-23.52	-38.53	-20.54	38.16	-12.02	-44.13	15.01	-2.64
PHMB-PHMB	-9.02	38.85	46.62	19.02	-7.19	-19.61	-47.86	-1.03
PHMB(Cl^-)-PHMB(Cl^-)	-15.97	-41.69	-39.03	51.59	-25.53	-28.72	25.72	-4.06

Supplementary Note 8 Molecular dynamics simulation

Although appropriate functionals combined with suitable basis sets can accurately describe the characteristics of atomic-level adsorption reactions, they overlook the molecular-scale dynamics of these reactions. To study the flocculation process at multiple scales, molecular adsorption processes in solution were dynamically simulated by GROMACS/2023 software using the GAFF force field[60,61]. After model construction, all systems underwent energy minimization to relax their structures fully. Subsequently, a 500 ps pre-simulation was performed at 298.15 K within a 25×25×25 nm box. A formal long-duration dynamic simulation in the NPT ensemble for 1000 ns followed. The formal simulation employed the Parrinello-Rahman method to control pressure, while the pre-progresses used the Berendsen method of pressure-bath coupling. The isothermal compressibility (k) for all systems was set to 4.5 e^{-5}•bar^{-1}, and the temperature was maintained at 298.15 K using the velocity rescaling thermostat. All systems' reference pressure (ref-p) was fixed as 1 bar. The coupling time constant (tau-p) for pressure control was set to 2.0 ps for the formal simulation and 0.5 ps for the pre-equilibration, respectively. The particle-mesh Ewald (PME) method was used to compute electrostatic interactions with a cutoff scheme implemented as the Verlet algorithm. The vdW interactions were calculated (vdwtype = cut-off) with a vdW interaction distance (rvdw) of 1.2 nm. The long-range corrections for energy and pressure were applied using the EnerPres approach. Additionally, hydrogen bonds in all systems were constrained to prevent excessive stretching or compression. The pre-equilibration and formal simulations employed periodic boundary conditions (PBC) in the x, y, and z directions. To refine the topology parameters for each molecule in the force field, optimization calculations and vibrational analysis were performed based on the M06-2X density functional with ma-def2-TZVP level by the Gaussian software to generate high-quality wavefunction files. The Sobtop program was used to directly calculate bond and angle parameters based on high-quality Hessian matrices, while other parameters (dihedral and improper) were obtained from the force field files[62]. Any missing parameters were also calculated based on the Hessian matrix to ensure the rotational flexibility of dihedral angles. The Multiwfn program provided RESP (restrained electrostatic potential) charge information for all atoms used in all molecular dynamics simulations[45,63]. Detailed information can be found in supplementary materials (MD.zip). An improved OPC3 water model was employed by optimizing the water model dipole moments[64]. In order to neutralize the charge of the system, only a corresponding number of counter ions were added to the simulation of aqueous solution (SOL: H_2O), while a large number of

Na^+ and Cl^- ions were added until the salt concentration reached 0.5 M to the simulation of salt solution (SOL: NaCl).

Supplementary Note 9

The findings illustrated in Supplementary Fig. 5e and Supplementary Fig. 19 showed that the frames associated with the lowest Gibbs energy consistently corresponded to the close bonding state. Moreover, the configuration corresponding to the PHMB-Dye binding was similar to that obtained from DFT calculations, both of which showed closely adhered complexes.

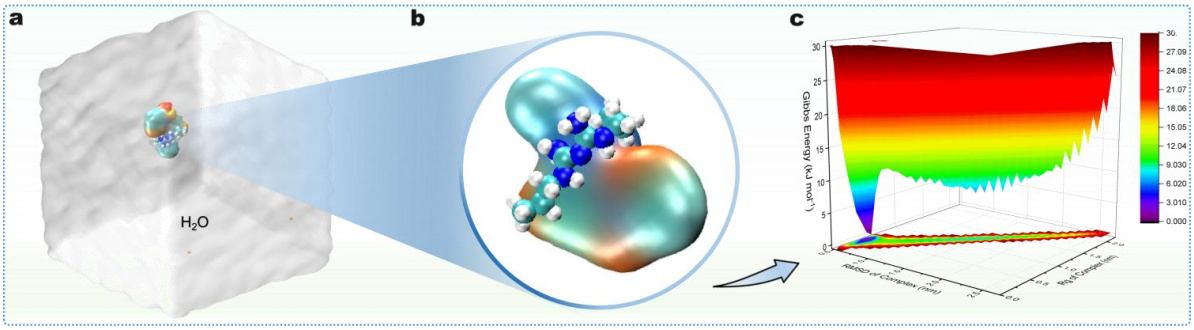

Supplementary Fig. 19 The model system for PHMB-Dye complex during the MD simulation. (a) A model system for PHMB-Dye complex in a water box. The configuration extracted from one frame (frame number 439861: about 880 ns) with the lowest Gibbs energy during the dynamic process in water solution **(b)** and corresponding free energy topography **(c)** in which RMSD and Rg of the PHMB-Dye complex as X value and Y value respectively.

Supplementary Table 3 MM/PBSA(Molecular mechanics/Poisson−Boltzmann Surface Area) calculations for the average gas-phase free energies, solvation free energies, and total binding energies in different complex systems calculated by the gmx_MMPBSA tool.

Complexes	istrng=0.15, fillratio=4.0, radiopt=0 (kcal/mol)					
	solvent	ΔG_{Gas}	ΔE_{Solv}	ΔE_{Total}	stratframe	endframe
PHMB-Dye	H_2O	-163.5	150.54	-12.96	375000	385000
PHMB-Dye	0.5 M NaCl	-156.78	145.51	-11.27	375000	385000
PHMB-PHMB	H_2O	4.03	-3.97	0.05	375000	385000
PHMB-PHMB	0.5 M NaCl	4.61	-4.55	0.06	375000	385000

Supplementary Note 10

Based on the data presented in Supplementary Figs. 20a, 20b, 20c, the overall properties of the simulated systems, including total energy, volume, density, temperature, and pressure, remained stable throughout the 1000 ns formal dynamics simulation. Under identical simulation conditions, the system in the sodium chloride solution exhibited lower total energy, larger volume, smaller density, and reduced pressure. These observations suggested a more stable system could be established in the presence of sodium chloride. For the PHMB monomer, the dye molecule, and their complex, values of RMSD (Root Mean Square Deviation) in Supplementary Figs. 20d, 20e, 20f and R_g (Radius of gyration) in Supplementary Figs. 20g, 20h, 20i fluctuated within the same range in both water and NaCl solution, showing no significant differences.

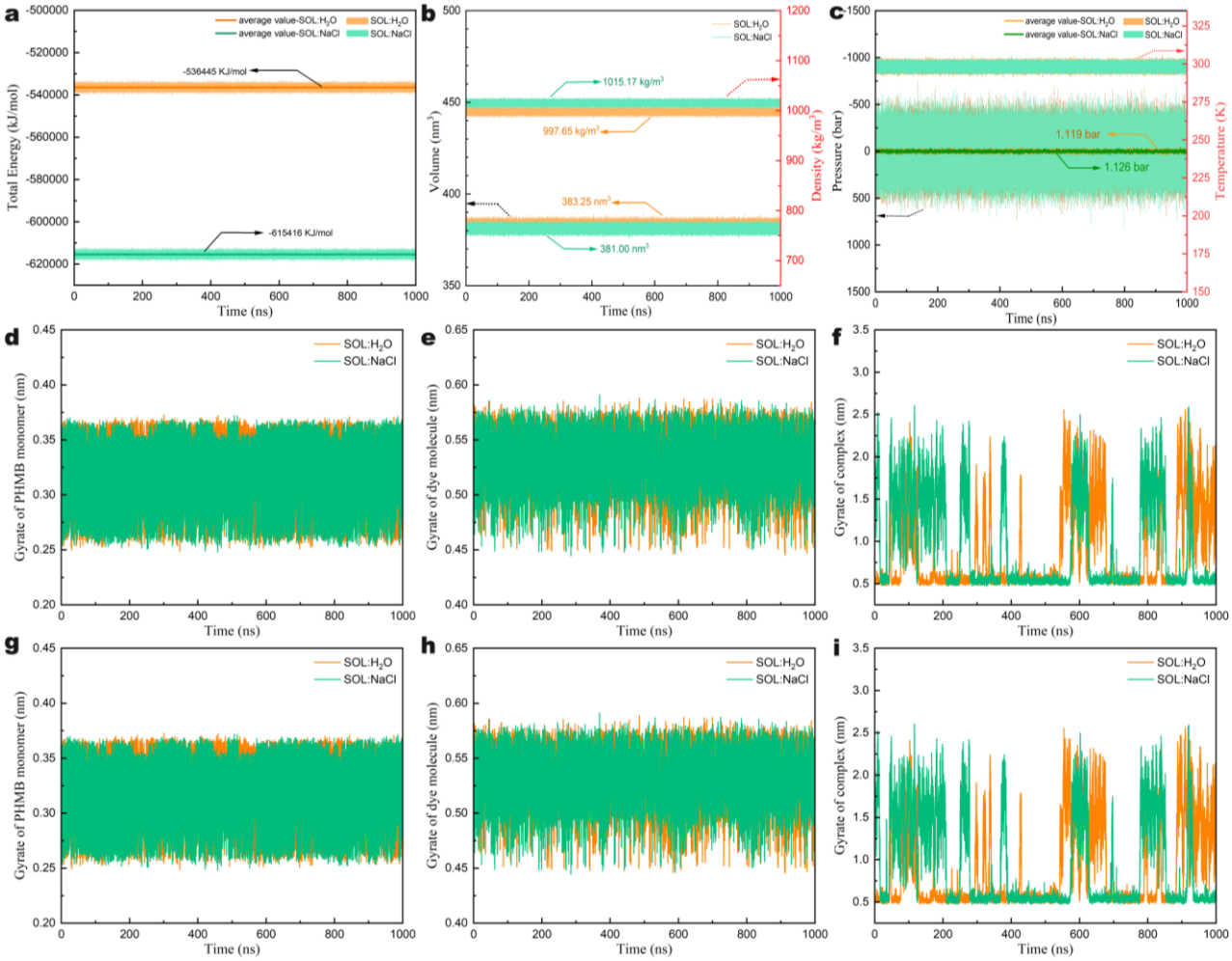

Supplementary Fig. 20 Comparison of overall properties of simulated systems. The total energy **(a)**, volume **(b)**, density **(b)**, temperature **(c)**, and pressure **(c)** in water and NaCl solution, respectively, during the 1000 ns formal dynamics simulation; RMSD of PHMB monomer **(d)**, dye molecule **(e)** and their complex **(f)** in water and NaCl solution, respectively; Time evolution of the radius of gyration (R_g)

of the PHMB monomer **(g)**, dye molecule **(h)** and their complex **(i)** in water and NaCl solution, respectively.

Supplementary Note 11

Notably, as shown in Supplementary Fig. 21, whether in water or sodium chloride solution, the hydrophobic and hydrophilic surface areas of the PHMB-Dye complex were almost equal when adsorbed together. However, the hydrophobic area was greater than the hydrophilic area when desorbed. This suggested that the adsorbed state that reduced the hydrophobic area was more favored, which was also evidenced by the significantly longer adsorption duration compared to desorption.

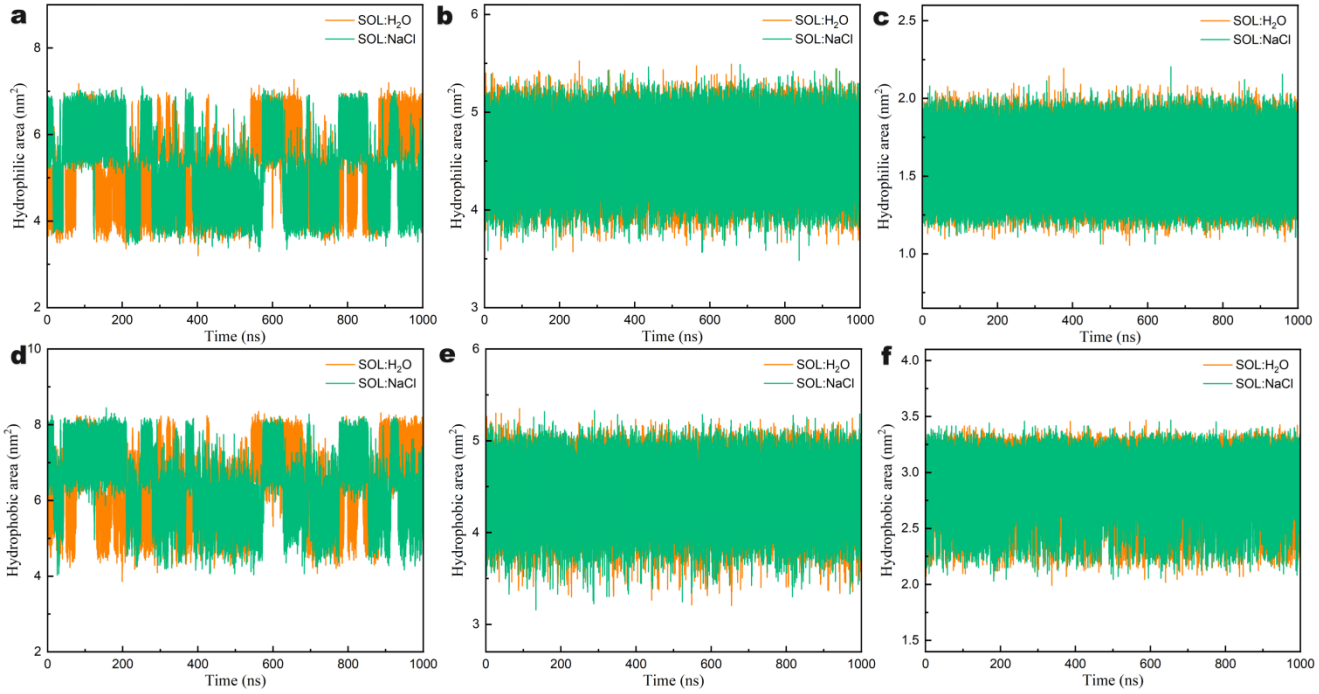

Supplementary Fig. 21 The hydrophobic and hydrophilic area of PHMB-Dye complex in the MD system. Hydrophobic area **(a, b, c)** and hydrophilic area **(d, e, f)** of PHMB-Dye complex **(a, d)**, the dye molecule **(b, e)**, and the PHMB monomer **(c. f)** in water and NaCl solution, respectively.

Supplementary Note 12

The weak interactions reflected by LJ-SR (short-range Lennard-Jones potential) were minimally affected by the addition of ions, suggesting that inorganic salt ions could hardly influence the weak interactions, which was vital for maintaining intermolecular binding (Supplementary Fig. 22). These findings indicated that, at least for the PHMB monomer, the weak-interaction adsorption mechanism for PHMB was resistant to the electrostatic shielding effect of inorganic ions.

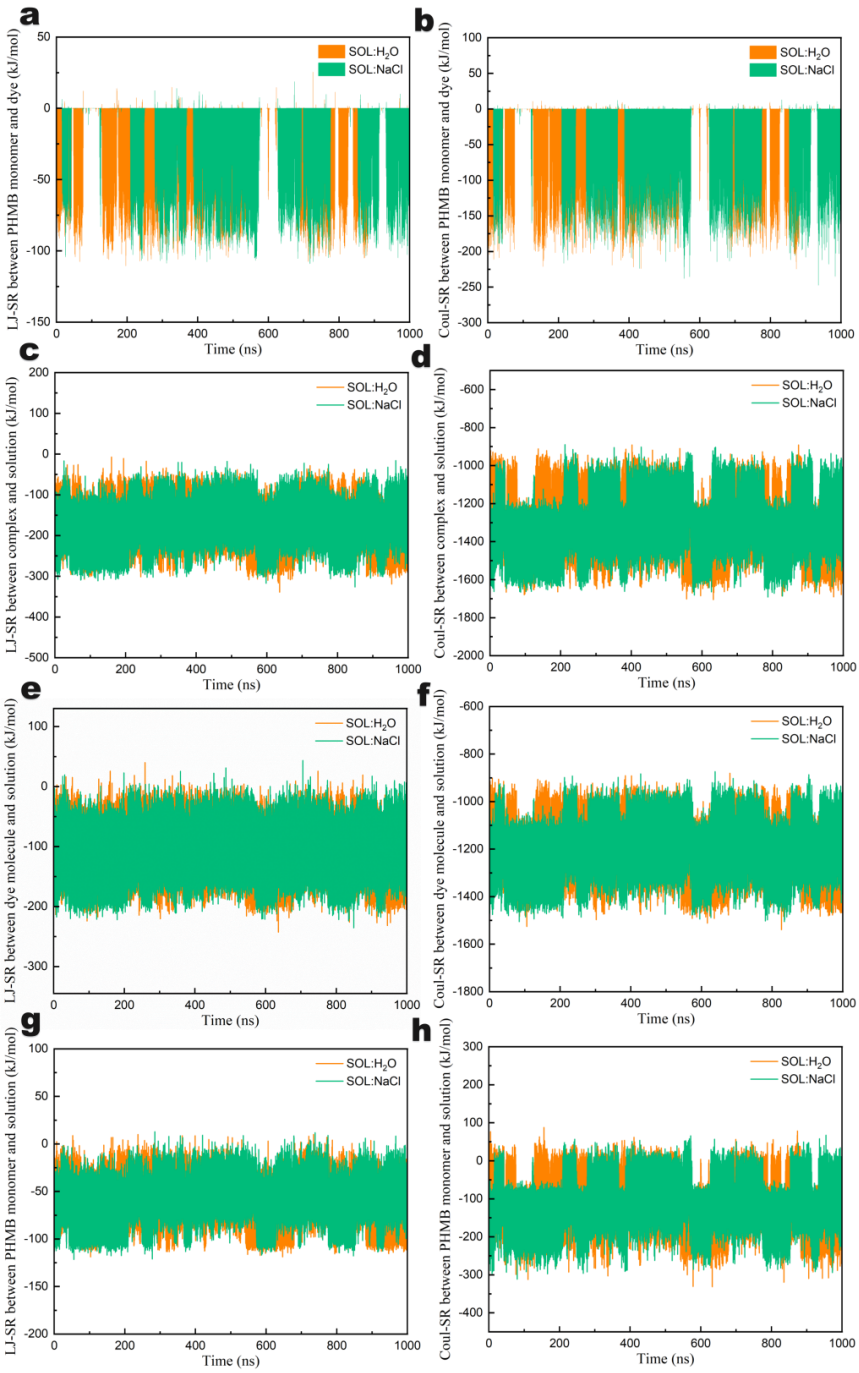

Supplementary Fig. 22 Coul-SR (short-range Coulomb interaction energy) and LJ-SR (short-range Lennard-Jones potential) of the PHMB-Dye MD system. Coul-SR (left) and LJ-SR (right) between PHMB monomer and dye molecule **(a, b)**, or two-molecule complex and solution **(c, d)**, or PHMB monomer and solution **(e, f)**, or dye molecule and solution **(g, h)**.

Supplementary Note 13

Although the average Coul-SR (short-range Coulomb interaction energy) value between PHMB and dye molecules increased by 2.67 kJ·mol^{-1} in NaCl and the average Coul-SR interaction between PHMB-Dye complex and NaCl solution was decreased by 4.78 kJ·mol^{-1}, the LJ-SR values hardly influenced by

salt ions, reflecting resistibility to charge shielding effect on the weak-interactions-dependent binding of PHMB and the dye (Supplementary Table 4).

Supplementary Table 4 The average Coul-SR and LJ-SR between PHMB monomer and dye molecule, or two-molecule complex and solution (Water_and_ions) or PHMB monomer and solution, or dye molecule and solution.

Object1	Object2	Water		0.5 M NaCl	
		Average Coul-SR (kJ/mol)	Average LJ-SR (kJ/mol)	Average Coul-SR (kJ/mol)	Average LJ-SR (kJ/mol)
PHMB	Dye	-45.00	-34.89	-42.33	-34.30
PHMB-Dye complex	Water_and_ions	-1305.47	-178.05	-1310.25	-178.42
PHMB	Water_and_ions	-106.08	-64.745	-108.56	-64.64
Dye	Water_and_ions	-1199.39	-113.30	-1201.69	-113.78

Supplementary Note 14 Screening-enhanced effect of PHMB in real dyeing wastewater

In order to test the flocculation performance of PHMB in actual red dyeing system, we collected wastewater from textile dyeing with different salt concentrations to replace the previous dye solution. The increment in colour removal efficiency resulting from increasing NaCl concentration could be defined as:

$$I_{salt}(\%) = \frac{R_{salt} - R_{nosalt}}{R_{nosalt}} \times 100\% \qquad (15)$$

Where the R_{salt} and R_{nosalt} were the colour removal efficiency at a certain NaCl concentration and 0 mmol·L^{-1}1 of NaCl, respectively. The economized quantity of PHMB Q_E caused by the addition of inorganic salt ions could be calculated as:

$$Q_E(\%) = \frac{Q_{salt} - Q_{nosalt}}{Q_{nosalt}} \times 100\% \qquad (16)$$

Where the Q_{salt} and Q_{nosalt} were the dye removal quantity at a certain NaCl concentration and 0 mmol·L^{-1} of NaCl, respectively.

Supplementary References

1. Frisch, M. J. *et al.* Gaussian˜16 Revision B.01. (2016).

2. Stephens, P. J., Devlin, F. J., Chabalowski, C. F. & Frisch, M. J. Ab Initio Calculation of Vibrational Absorption and Circular Dichroism Spectra Using Density Functional Force Fields. *J. Phys. Chem.* **98**, 11623–11627 (1994).

3. Becke, A. D. Density-functional exchange-energy approximation with correct asymptotic behavior. *Phys. Rev. A* **38**, 3098–3100 (1988).

4. Lee, C., Yang, W. & Parr, R. G. Development of the Colle-Salvetti correlation-energy formula into a functional of the electron density. *Phys Rev B* **37**, 785–789 (1988).

5. Grimme, S., Ehrlich, S. & Goerigk, L. Effect of the damping function in dispersion corrected density functional theory. *J. Comput. Chem.* **32**, 1456–1465 (2011).

6. Grimme, S., Antony, J., Ehrlich, S. & Krieg, H. A consistent and accurate ab initio parametrization of density functional dispersion correction (DFT-D) for the 94 elements H-Pu. *J. Chem. Phys.* **132**, 154104 (2010).

7. Schäfer, A., Horn, H. & Ahlrichs, R. Fully optimized contracted Gaussian basis sets for atoms Li to Kr. *J. Chem. Phys.* **97**, 2571–2577 (1992).

8. Schäfer, A., Huber, C. & Ahlrichs, R. Fully optimized contracted Gaussian basis sets of triple zeta valence quality for atoms Li to Kr. *J. Chem. Phys.* **100**, 5829–5835 (1994).

9. Glendening, E. D., Reed, A. E., Carpente, J. E. & Weinhold, F. NBO Version 3.1.

10. Naaman, Ron. & Zeev, Vager. *The structure of small molecules and ions*. (Plenum Press, 1988).

11. Carpenter, J. E. & Weinhold, F. Analysis of the geometry of the hydroxymethyl radical by the "different hybrids for different spins" natural bond orbital procedure. *J. Mol. Struct. THEOCHEM* **169**, 41–62 (1988).

12. Carpenter, J. E. *Extension of Lewis structure concepts to open-shell and excited- state molecular species*. ([Place of publication not identified] : [publisher not identified], 1987., 1987).

13. Reed, A. E., Curtiss, L. A. & Weinhold, F. Intermolecular interactions from a natural bond orbital, donor-acceptor viewpoint. *Chem. Rev.* **88**, 899–926 (1988).

14. Reed, A. E. & Weinhold, F. Natural bond orbital analysis of near-Hartree–Fock water dimer. *J. Chem. Phys.* **78**, 4066–4073 (1983).

15. Reed, A. E. & Weinhold, F. Natural localized molecular orbitals. *J. Chem. Phys.* **83**, 1736–1740 (1985).

16. Reed, A. E., Weinstock, R. B. & Weinhold, F. Natural population analysis. *J. Chem. Phys.* **83**, 735–746 (1985).

17. Foster, J. P. & Weinhold, F. Natural hybrid orbitals. *J. Am. Chem. Soc.* **102**, 7211–7218 (1980).

18. Zhao, Y. & Truhlar, D. G. The M06 suite of density functionals for main group thermochemistry, thermochemical kinetics, noncovalent interactions, excited states, and transition elements: two new functionals and systematic testing of four M06-class functionals and 12 other functionals. *Theor. Chem. Acc.* **120**, 215–241 (2008).

19. Weigend, F., Häser, M., Patzelt, H. & Ahlrichs, R. RI-MP2: optimized auxiliary basis sets and demonstration of efficiency. *Chem. Phys. Lett.* **294**, 143–152 (1998).

20. Weigend, F. & Ahlrichs, R. Balanced basis sets of split valence, triple zeta valence and quadruple zeta valence quality for H to Rn: Design and assessment of accuracy. *Phys. Chem. Chem. Phys.* **7**, 3297–3305 (2005).

21. Zheng, J., Xu, X. & Truhlar, D. G. Minimally augmented Karlsruhe basis sets. *Theor. Chem. Acc.* **128**, 295–305 (2011).

22. Weigend, F. Accurate Coulomb-fitting basis sets for H to Rn. *Phys. Chem. Chem. Phys.* **8**, 1057–1065 (2006).

23. Marenich, A. V., Cramer, C. J. & Truhlar, D. G. Universal Solvation Model Based on Solute Electron Density and on a Continuum Model of the Solvent Defined by the Bulk Dielectric Constant and Atomic Surface Tensions. *J. Phys. Chem. B* **113**, 6378–6396 (2009).

24. Hafner, J. Ab-initio simulations of materials using VASP: Density-functional theory and beyond. *J. Comput. Chem.* **29**, 2044–2078 (2008).

25. Kresse, G. & Furthmüller, J. Efficiency of ab-initio total energy calculations for metals and semiconductors using a plane-wave basis set. *Comput. Mater. Sci.* **6**, 15–50 (1996).

26. Perdew, J. P., Burke, K. & Ernzerhof, M. Generalized Gradient Approximation Made Simple. *Phys. Rev. Lett.* **77**, 3865–3868 (1996).

27. Kresse, G. & Furthmüller, J. Efficient iterative schemes for ab initio total-energy calculations using a plane-wave basis set. *Phys. Rev. B* **54**, 11169–11186 (1996).

28. Mathew, K., Sundararaman, R., Letchworth-Weaver, K., Arias, T. A. & Hennig, R. G. Implicit solvation model for density-functional study of nanocrystal surfaces and reaction pathways. *J. Chem. Phys.* **140**, 084106 (2014).

29. Mathew, K., Kolluru, V. S. C., Mula, S., Steinmann, S. N. & Hennig, R. G. Implicit self-consistent electrolyte model in plane-wave density-functional theory. *J. Chem. Phys.* **151**, 234101 (2019).

30. Lu, T. & Chen, F. Multiwfn: A multifunctional wavefunction analyzer. *J. Comput. Chem.* **33**, 580–592 (2012).

31. Humphrey, W., Dalke, A. & Schulten, K. VMD: Visual molecular dynamics. *J. Mol. Graph.* **14**, 33–38 (1996).

32. Momma, K. & Izumi, F. VESTA 3 for three-dimensional visualization of crystal, volumetric and morphology data. *J. Appl. Crystallogr.* **44**, 1272–1276 (2011).

33. Tang, W., Sanville, E. & Henkelman, G. A grid-based Bader analysis algorithm without lattice bias. *J. Phys. Condens. Matter Inst. Phys. J.* **21**, 084204 (2009).

34. Henkelman, G., Arnaldsson, A. & Jónsson, H. A fast and robust algorithm for Bader decomposition of charge density. *Comput. Mater. Sci.* **36**, 354–360 (2006).

35. Sanville, E., Kenny, S. D., Smith, R. & Henkelman, G. Improved grid-based algorithm for Bader charge allocation. *J. Comput. Chem.* **28**, 899–908 (2007).

36. Yu, M. & Trinkle, D. R. Accurate and efficient algorithm for Bader charge integration. *J. Chem. Phys.* **134**, 064111 (2011).

37. Watanabe, T., Manz, T. A. & Sholl, D. S. Accurate Treatment of Electrostatics during Molecular Adsorption in Nanoporous Crystals without Assigning Point Charges to Framework Atoms. *J. Phys. Chem. C* **115**, 4824–4836 (2011).

38. Manz, T. A. & Sholl, D. S. Chemically Meaningful Atomic Charges That Reproduce the Electrostatic Potential in Periodic and Nonperiodic Materials. *J. Chem. Theory Comput.* **6**, 2455–2468 (2010).

39. Manz, T. A. & Sholl, D. S. Methods for Computing Accurate Atomic Spin Moments for Collinear and Noncollinear Magnetism in Periodic and Nonperiodic Materials. *J. Chem. Theory Comput.* **7**, 4146–4164 (2011).

40. Manz, T. A. & Sholl, D. S. Improved Atoms-in-Molecule Charge Partitioning Functional for Simultaneously Reproducing the Electrostatic Potential and Chemical States in Periodic and Nonperiodic Materials. *J. Chem. Theory Comput.* **8**, 2844–2867 (2012).

41. Manz, T. A. & Limas, N. G. Introducing DDEC6 atomic population analysis: part 1. Charge partitioning theory and methodology. *RSC Adv.* **6**, 47771–47801 (2016).

42. Limas, N. G. & Manz, T. A. Introducing DDEC6 atomic population analysis: part 2. Computed results for a wide range of periodic and nonperiodic materials. *RSC Adv.* **6**, 45727–45747 (2016).

43. Manz, T. A. Introducing DDEC6 atomic population analysis: part 3. Comprehensive method to compute bond orders. *RSC Adv.* **7**, 45552–45581 (2017).

44. Lu, T. & Chen, F. Quantitative analysis of molecular surface based on improved Marching Tetrahedra algorithm. *J. Mol. Graph. Model.* **38**, 314–323 (2012).

45. Zhang, J. & Lu, T. Efficient evaluation of electrostatic potential with computerized optimized code. *Phys. Chem. Chem. Phys.* **23**, 20323–20328 (2021).

46. Dennington, R., Keith, T. A. & Millam, J. M. GaussView Version 6.0.16. (2016).

47. Suresh, C. H., Remya, G. S. & Anjalikrishna, P. K. Molecular electrostatic potential analysis: A

powerful tool to interpret and predict chemical reactivity. *WIREs Comput. Mol. Sci.* **12**, (2022).

48. Murray, J. S. & Politzer, P. The electrostatic potential: an overview. *WIREs Comput. Mol. Sci.* **1**, 153–163 (2011).

49. Politzer, P. & Murray, J. S. The fundamental nature and role of the electrostatic potential in atoms and molecules. *Theor. Chem. Acc. Theory Comput. Model. Theor. Chim. Acta* **108**, 134–142 (2002).

50. Mulliken, R. S. Electronic Population Analysis on LCAO–MO Molecular Wave Functions. I. *J. Chem. Phys.* **23**, 1833–1840 (2004).

51. Henkelman, G., Uberuaga, B. P. & Jónsson, H. A climbing image nudged elastic band method for finding saddle points and minimum energy paths. *J. Chem. Phys.* **113**, 9901–9904 (2000).

52. Wang, V., Xu, N., Liu, J.-C., Tang, G. & Geng, W.-T. VASPKIT: A user-friendly interface facilitating high-throughput computing and analysis using VASP code. *Comput. Phys. Commun.* **267**, 108033 (2021).

53. Manz, T. A. & Limas, N. G. Chargemol Version 3.5. (2017).

54. Johnson, E. R. *et al.* Revealing Noncovalent Interactions. *J. Am. Chem. Soc.* **132**, 6498–6506 (2010).

55. Lu, T. & Chen, Q. Visualization Analysis of Weak Interactions in Chemical Systems. in *Reference Module in Chemistry, Molecular Sciences and Chemical Engineering* (Elsevier, 2023). doi:10.1016/B978-0-12-821978-2.00076-3.

56. Lefebvre, C. *et al.* Accurately extracting the signature of intermolecular interactions present in the NCI plot of the reduced density gradient versus electron density. *Phys. Chem. Chem. Phys.* **19**, 17928–17936 (2017).

57. Lu, T. & Chen, Q. Independent gradient model based on Hirshfeld partition: A new method for visual study of interactions in chemical systems. *J. Comput. Chem.* **43**, 539–555 (2022).

58. Lu, T. & Chen, Q. *Erratum to "Independent gradient model based on Hirshfeld partition: A new method for visual study of interactions in chemical systems"*. https://chemrxiv.org/engage/chemrxiv/article-details/6356bf2dca86b856a3c1793e (2022) doi:10.26434/chemrxiv-2022-g1m34.

59. Geuenich, D., Hess, K., Köhler, F. & Herges, R. Anisotropy of the Induced Current Density (ACID), a General Method To Quantify and Visualize Electronic Delocalization. *Chem. Rev.* **105**, 3758–3772 (2005).

60. Abraham, M. J. *et al.* GROMACS: High performance molecular simulations through multi-level parallelism from laptops to supercomputers. *SoftwareX* **1**, 19–25 (2015).

61. Wang, J., Wolf, R. M., Caldwell, J. W., Kollman, P. A. & Case, D. A. Development and testing of a general amber force field. *J. Comput. Chem.* **25**, 1157–1174 (2004).

62. Lu, T. Sobtop Version 1.0. (2022).

63. Bayly, C. I., Cieplak, P., Cornell, W. & Kollman, P. A. A well-behaved electrostatic potential based method using charge restraints for deriving atomic charges: the RESP model. *J. Phys. Chem.* **97**, 10269–10280 (1993).

64. Izadi, S. & Onufriev, A. V. Accuracy limit of rigid 3-point water models. *J. Chem. Phys.* **145**, 074501 (2016).